ELSEVIER

High-performance CeO$_2$:Co nanostructures for the elimination of accidental poisoning caused by CO intoxication

J.C.L. Carvalho [a], L.S.R. Rocha [b,*], R.A. Renzetti [c], A.M.S. Procopio [a], V.R. Mastelaro [d], A.Z. Simões [e], M.A. Ponce [f], C. Macchi [g], A. Somoza [g], C.M. Aldao [h], E. Longo [b], F. Moura [a]

[a] Advanced Materials Interdisciplinary Laboratory, Federal University of Itajubá, (UNIFEI), Campus Itabira, MG, Brazil
[b] Center for Research and Development of Functional Materials, Federal University of São Carlos (UFSCar), São Carlos, SP, Brazil
[c] Institute of Integrated Engineering, Federal University of Itajubá(UNIFEI), Campus Itabira, MG, Brazil
[d] São Carlos Institute of Physics, University of São Paulo (USP), PO Box 369, 13560-970, São Carlos, SP, Brazil
[e] School of Engineering, São Paulo State University (UNESP), 333 Dr. Ariberto Pereira da Cunha Avenue, Portal das Colinas, 12516-410, Guaratinguetá, SP, Brazil
[f] National University of Mar del Plata (UNMdP), Buenos Aires, Argentina
[g] CIFICEN (UNCPBA-CICPBA-CONICET) and Instituto de Física de Materiales Tandil (UNCPBA), Pinto 399, B7000GHG, Tandil, Argentina
[h] Institute of Scientific and Technological Research in Electronics (ICYTE) University of Mar del Plata and National Research Council (CONICET), Mar del Plata, Argentina

ARTICLE INFO

ABSTRACT

Owing to the global upward trend of accidental carbon monoxide (CO) poisoning in the past 30 years, this work aimed to develop Cobalt-doped CeO$_2$ particles by the microwave-assisted hydrothermal route under distinct conditions. Their structural, morphological, spectroscopic and electrical behaviors were investigated to correlate the influence of Co on their properties with the introduction of oxygen vacancies and their sensing capability to assist in the mitigation of CO poisoning cases. The samples were crystalline and had no secondary phases. Two distinct activation energies for the electrical conduction processes were observed due to dopant influence, corroborating the local cluster-to-cluster charge transfer (CCCT) mechanism, resulting in a response time of only 3s for the 4% Co-doped sample. On the other hand, through positron annihilation studies we showed that the oxygen vacancies are preferentially formed near Co ions, reducing the Co ion charge and leading to the formation of neutral V$_O$-Co^{+2} complex clusters.

1. Introduction

The selective and highly sensitive detection of pollutant/toxic/explosive gases in industries and homes remains very challenging, especially because of the global upward trend of accidental carbon monoxide poisoning in the past 30 years [1].

For this reason, there are several works in the literature dealing with the detection and/or monitoring of low-level pollutant components [2–6], especially cerium dioxide (CeO$_2$),which is considered one of the most important oxides and a promising material for the environmental monitoring of atmospheres due to its unique physico-chemical properties resulting from the cycling between Ce^{3+}/Ce^{4+} oxidation states [7, 8].

Cerium is one of the most abundant rare-earth elements, with atomic number Z = 58 and electronic configuration [Xe] 4f^1 5 d^1 6s^2. Owing to its electropositivity, this element has two oxidation states, Ce(III)/Ce (IV) [9] which are intrinsically correlated to the gas detection performance of cerium dioxide (CeO$_2$)-based materials.

Such performance can be intensified through structural modification, with the presence of defects such as doping agents, which end up strongly influencing its behavior [10]. It was shown that the formation of oxygen vacancies(Vo¨) is accompanied by electron transfer from O 2p to Ce 4f orbitals, causing a reduction of Ce^{4+} to Ce^{3+} (Ce$'_{Ce}$) [11]. This reduction leads to the formation of a non-stoichiometric compound (CeO$_{2-x}$) that is fundamental for the oxygen storage capability as well as the electronic transport throughout the lattice [12].

Over the last years, our group has extensively studied the synthesis, properties, and applications of pure and rare-earth doped ceria nanostructures obtained via the MAH (microwave-assisted hydrothermal) method [13–18].

In this work, the modification with cobalt, obtained from cobalt oxide, can be expressed according to Equation (1):

$$CoO + 2CeO_2 \leftrightarrow Co_{Ce}'' + V_{\ddot{O}} + 5O_o^x + 2Ce_{Ce}^x, \tag{1}$$
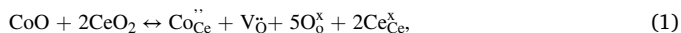
where Co_{Ce}'' represents the substitution of Ce^{4+} by Co^{2+}ion, $O_o^x$is the oxygen on its ground state and $V_{\ddot{O}}$is the doubly-ionized oxygen vacancy. As Co ions have a lower valence than that of Ce(IV) in the CeO_2, their introduction into the lattice tends to change the original electronic state of nanoparticles, thus affecting the content of Ce(III) as well as their adsorption property and sensing activity. We expected that the doping of CeO_2 with Co would excite its electrons, moving them to the conduction band of transition metals (Co), with the same number of holes appearing in the valence band. Furthermore, we proposed the introduction of cobalt, a transition metal, so as to improve the optical and sensing properties of nanoparticles towards CO by modifying their energy band structure and altering their morphology and surface-to-volume ratio, besides creating more active centers at grain boundaries. Moreover, this introduction allows the creation of oxygen vacancies to maintain the local charge balance, which in turn increases the redox activity, enhancing the ionic conductivity and improving the sensitivity of CeO_2 towards carbon monoxide.

The modification of ceria nanoparticles with Co was responsible for the catalytic performance improvement reported by Refs. [19,20] as well as the enhancement of the fuel cell performance [21]. Nanocomposites of Co–CeO_2 prepared by an electrodeposition process showed hierarchical cobalt nanoflake-like morphologies that enhanced the hydrazine electro-oxidation peak current (2.6 mA) and made them highly sensitivity for the amperometric sensing of hydrazine [1].

Regarding the electronic conduction of ceria-based materials, it can be assigned to the small polaron theory based on the hopping mechanism [22], with their quantum exchange interactions [23] controlling the overall phenomena. The charge transfer process is locally controlled by the cluster-to-cluster charge transfer (CCCT) mechanism, previously described by our group, with a probability that roughly depends on the distance between adjacent species [24]. With respect to the modification of the cerium oxide structure with transition metals, it was reported that the hybridization of orbitals facilitates the capture of electrons from oxygen defective structures with a consequent ease of the electrical conduction, as was the case of Mn-doped CeO_2 structures prepared by Nishimura et al. [25], as well as Cu-doped CeO_2 porous microspheres synthetized by Zhou et al. [26], which showed a higher catalytic activity for CO oxidation in comparison with the pure sample.

Therefore, in this work we prepared pure and Co-doped CeO_2 (4 and 12 wt%) by the microwave-assisted hydrothermal route to investigate the presence of structural defects due to modification with a transition metal, as well as its correlation with the gas-sensing behavior of the nanoparticles under a carbon monoxide atmosphere in order to assist in the mitigation of unintentional intoxication cases worldwide. To this end, we analyzed their structural, morphological and optical properties via X-ray diffraction (XRD), Raman spectroscopy, ultraviolet–visible spectroscopy (UV–Vis), infrared spectroscopy (FT-IR), positron annihilation lifetime spectroscopy (PALS), X-ray photoelectron spectroscopy (XPS), and scanning electron microscopy (SEM).

2. Experimental procedures

2.1. Powders synthesis and characterizations

The powders were prepared by the microwave-assisted hydrothermal (MAH) route with a modification of 4 and 12 wt% of cobalt. First, cerium nitrate hexahydrate ($Ce(NO_3)_3 \cdot 6H_2O$) and cobalt nitrate hexahydrate ($Co(NO_3)_2 \cdot 6H_2O$) solutions were separately dissolved in distilled water at 70 °C under constant stirring. Then, the former solutions were mixed, had their pH adjusted to 10 using a 2 M KOH solution and taken to the microwave. In the microwave equipment, the solutions
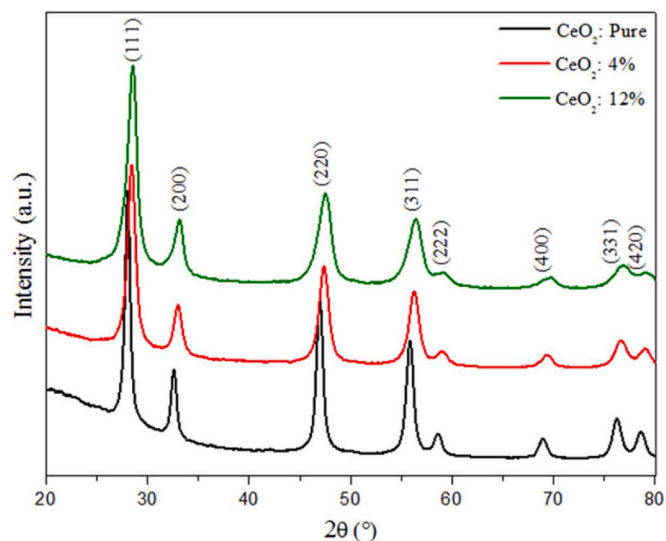

Fig. 1. XRD results of the pure and Co-doped samples obtained by the MAH route.

were heated up to 100 °C (synthesis temperature), using a heating rate of 10°/min, and kept in this temperature for 8 min (synthesis time). The solutions were cooled down to room temperature and taken to characterizations. X-ray diffraction (XRD) measurements were performed on a Rigaku RINT 2000 diffractometer (40 kV, 30 mA) with Cu-Kα radiation ($\lambda = 1.5406$ Å) at a scan speed of 0.2°/s from 20 to 110°. Chebyshev polynomial and pseudo-Voigt function were used for background correction and peak fitting, respectively, during the Rietveld refinement analysis (Supplementary Information). Raman spectroscopy measurements were carried out with 32 scans using a HORIBA Synapse charge-coupled detector (CCD) equipped with a Nd-YAG laser ($\lambda = 514{,}5$ nm) at 100 mW and a spectral resolution of 4 cm^{-1}. Ultraviolet–visible (UV–Vis) spectroscopy was performed on a SHIMADZU UV-2600 spectrometer in diffuse reflectance mode from 185 to 1400 nm (Supplementary Information). Fourier-transform infrared (FT-IR) spectroscopy was carried out using Vertex 70 equipment (Bruker, Massachusetts)in attenuated total reflectance (ATR) mode from 4000 to 500 $cm^{-1}$and at a spectral resolution of 1 cm^{-1} (Supplementary Information). X-ray photoelectron spectroscopy (XPS) measurements were performed on a Scienta Omicron ESCA + spectrometer operating at a constant energy rate of 50 eV equipped with an EA125 hemispherical analyzer and a monochromatic Al Kα source (hν = 1486.7 eV; 280 W), using CASA XPS software (Casa Software Ltd, UK) for data analysis. For XPS measurements, samples in powder form were deposited on a conductive double-sided carbon tape. To avoid spurious signals from the carbon tape, the surface of the tape was completely covered by the sample. The measurements were performed in vacuum at 1×10^{-9}mbar. Scanning electron microscopy (SEM) images were obtained with the aid of FEG-SEM Supra 35-VP equipment operating at an accelerating voltage of 5 kV. Positron annihilation lifetime spectroscopy (PALS) spectra were obtained using a fast–fast system in a collinear geometry with a time resolution of 275 ps. As a positron source, a 10 μCi sealed source of ^{22}NaCl deposited onto two thin Kapton foils (7.5-μm thick) sandwiched between two identical samples was used. The spectra were acquired at room temperature, and ~1.5–2 $\times 10^6$ counts per spectrum were collected. The lifetime values reported herein for each sample are at least an average of 10 measurements under the same experimental conditions. After subtracting the background and the source contribution, the positron lifetime spectra were analyzed using the LT10 program [27].
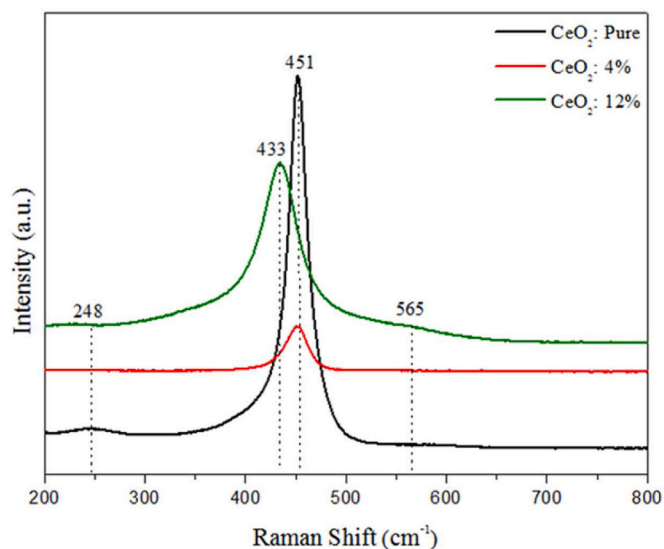
Fig. 2. Raman spectra for the pure and Co-doped CeO_2 nanopowders.

Table 1
Stoichiometric composition of the samples from energy regions: C(1s), O(1s), Ce (3d), and Co(2p).

Elements	CeO$_2$: Pure	CeO$_2$: 4% Co	CeO$_2$: 12% Co
Carbon (C)	51.7%	48.3%	49.8%
Oxygen (O)	37.2%	34.0%	34.9%
Cerium (Ce)	11.1%	17.8%	13.8%
Cobalt (Co)	0%	-*	1.5%

2.2. Films preparation and characterization

The thick films were prepared by a simple screen-printing-like deposition process for the electrical measurements, according to previous publications [4,15].

The electrical measurements in vacuum, air and carbon monoxide (CO) atmospheres were carried out using an Agilent 3440 multimeter at a direct current (DC) of 1 mA coupled to a Keithley 6514 electrometer in a device for optoelectronic characterization of materials [28,29].

3. Results and discussion

3.1. Nanoparticles characterization

3.1.1. XRD measurements

The XRD analyses of nanoparticles in Fig. 1 show that both samples have a cubic polycrystalline structure of CeO_2, spatial group *Fm-3m*, ICSD no. 72155 [30]. The presence of high-intensity peaks closely related to mean crystallite sizes can be clearly observed, besides a certain broadening that can be attributed to the dopant concentration increase. In other words, the broader the peaks, the smaller the mean crystallite size [31]. A shift of the main CeO_2 peaks with increasing the dopant concentration related to the formation of a solid solution with a distinct ionic radius (Co^{2+} 0.75 Å and Ce^{3+} 1.03 Å) can also be noted [32,33]. Additionally, no secondary phases were identified, which is indicative of a polycrystalline material formation that respects its solubility limits, according to the Hume–Rothery rules [34].

Kumar et al. [35] prepared Co/CeO_2 nanofibers with distinct weight percentages of cobalt (1, 5, and 10 wt%) and observed no significant change in the XRD peaks, except for some very small peak shifts. According to the authors, the 10 wt% Co/CeO2 sample (the richest in Co) was characterized by the appearance of additional peaks that corresponded to the Co_3O_4 phase indicated in JCPDS card no. 78–1970.

Thus, we can conclude that the MAH route was able to promote the formation of pure and Co-doped crystalline cerium dioxide particles at a low temperature (100 °C) and a reduced synthesis time (8min).

3.1.2. Raman spectroscopy

Raman spectroscopy was carried out to investigate the phase formation, short-range order-disorder, and structural defects of the different Co-doped ceria nanostructures (Fig. 2). It is reported that dioxides with a fluorite-like cubic structure have only one active mode derived from F_{2g} symmetry in the Raman spectra due to the symmetric

axial deformation of $[CeO_8]$ species [36]. Usually, when a dopant with a +2 effective charge is introduced, a charge imbalance is generated. In order to balance the excessive charge, oxygen vacancies are created, accompanied by the Ce(IV) → Ce(III) reduction [37]. For the pure system, this band is generally around 465 cm^{-1} [38].

As observed, there is a shift of the F_{2g} mode towards lower energies from 451 to 433 cm^{-1} with increasing the Co content, which corroborates the presence of oxygen vacancies and their increased amount as the doping increases.

It is worth mentioning that the oxidation state and ionic radius changes influence the peak position by altering the short-range order of the system. In ceria-based compounds, oxygen vacancies originate from two main sources: Co^{3+} or Co^{2+} doping cations replacing the host Ce^{4+} and the non-stoichiometry associated with the intrinsic reduction of Ce^{4+} to Ce^{3+}. In both cases, charge differences between the substituting cations (Co^{3+}, Co^{2+}, or Ce^{3+}) and Ce^{4+} create oxygen vacancies to maintain charge neutrality, resulting in a weak Raman mode around 600 cm^{-1}. One can also estimate the relative oxygen vacancy concentration in the samples by calculating the ratio between the intensities of the oxygen vacancy mode (I_D) and the F_{2g} mode (I_{F2g}) [39].

The other two low intensity bands around 565 cm^{-1} and 248 cm^{-1} are related to A_{1g} (LO) and E_g (TO), respectively. According to the literature, they are associated with intrinsic defects such as oxygen vacancies [40], which are commonly found in nanostructured materials [41]. The absence of modes belonging to precursors or intermediary products (e.g., CoO or Co_2O_3) reinforces that the samples are crystalline, with no signs of secondary phases detected in their Raman spectra.

3.1.3. X-rays photoelectron spectroscopy (XPS)

The elements and the estimated concentration from the XPS spectra can be seen in Table 1.

Despite the ultra-high vacuum atmosphere in which the samples were measured, it is common to find C 1s spectra around 50%due to saturated hydrocarbons [42,43]. Additionally, for the 12 wt% sample the amount of Co ions on its surface was less than 2%.

For a deeper analysis, we collected high-resolution spectra of Ce 3d species (Fig. 3). According to Fig. 3(a), few differences can be observed in the Ce 3d spectra when cobalt is added to CeO_2. The peak situated around 917 eV is characteristic of Ce^{4+} oxidation state and is present in all the samples [44]. The literature reports that the XPS spectrum of CeO_2 compound can be deconvoluted into 6 components. However, Fig. 3(b) shows that the XPS spectrum of CeO_2 was deconvoluted into 8 components, suggesting the presence of Ce^{3+} and Ce^{4+} species and the hybridization of energy levels [45,46]. The components located between 880 and 904 eV correspond to the Ce 3d$_{5/2}$ level, while those between 905 and 917 eV refer to Ce 3d$_{3/2}$. The three peaks around 882–883, 889–890 and 898–899 eV can be attributed to Ce^{4+} species, while the other two components around 881–882 and 885–886 eV can be assigned to Ce^{3+} oxidation state [47,48]. The peak around 917 eV is characteristic of the Ce(IV), showing that the Ce^{4+} oxidation state is predominant in the three studied samples.

Fig. 4 depicts the Co 2p high-resolution XPS spectrum of the sample doped with 12 wt% Co, which is characterized by three peaks located around 780, 785, and 796 eV, corresponding to Co 2p$_{3/2}$, the satellite peak characteristic of cobalt and Co 2p$_{1/2}$ levels, respectively. The deconvolution process showed that the Co 2p$_{3/2}$ level is formed by two
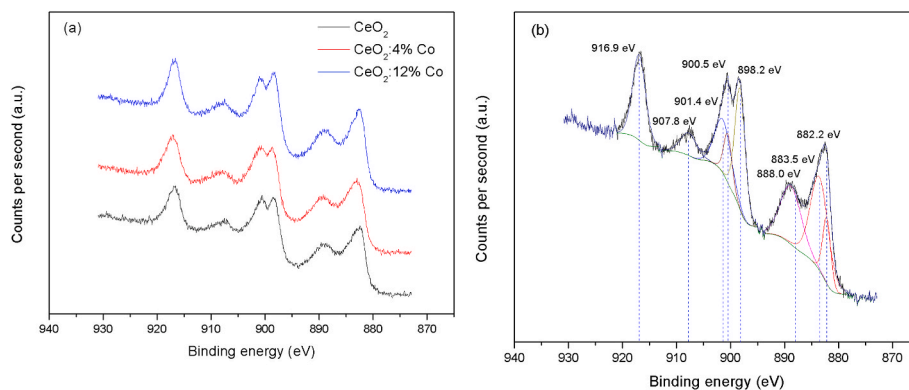
Fig. 3. (a) Ce 3d high-resolution XPS spectra of pure and Co doped samples and (b) deconvoluted Ce 3d high-resolution XPS spectra of 12% wt. sample.
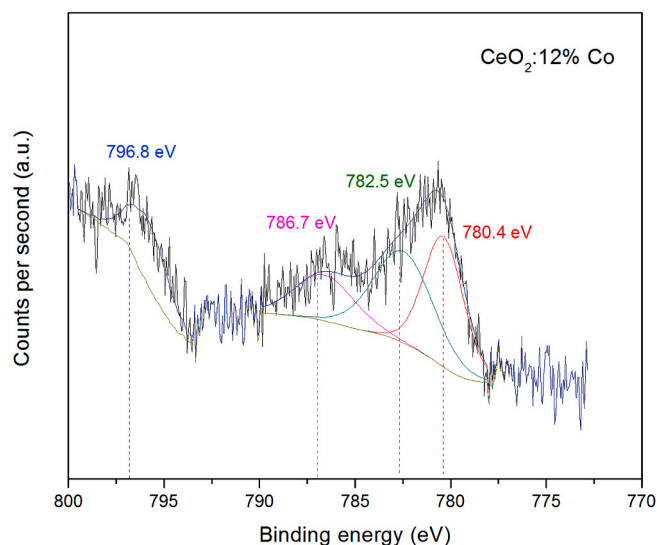

Fig. 4. High-resolution XPS spectra on the Co 2p region of the 12% wt. Sample.

components with energies of 780.4, and 782.5 eV associated with the presence of Co^{3+} and Co^{2+} [49] with approximately the same proportion (50% each).

According to the XPS measurements, it was not possible to determine the variation of the Ce(III)/Ce(IV) configuration as a function of cobalt addition, with the Ce(IV) configuration being the dominant entity. However, the variation of cobalt oxidation states referring to Co^{2+} and Co^{3+} obtained was found to be probably responsible for the contribution of Co 3d levels to the electrical conduction mechanisms and cluster-to-cluster charge transfer (CCCT) processes.

3.1.4. Field-emission gun scanning electron microscopy (FEG-SEM)

Fig. 5 shows the FEG-SEM images of the pure and Co-doped ceria nanostructures synthesized by the microwave-assisted hydrothermal method. The micrographies reveal undefined morphologies with a high degree of agglomeration, besides a reduction in the mean aggregate sizes with increasing the Co content. According to Table 2, the sizes of these morphologies range between 50.15 and 43.24 nm. It is worth noting that for all samples the nanostructures formed large agglomerates. This phenomenon is common for nanomaterials, especially when surfactants are not used in the synthesis. Owing to the nanometric nature of the particles, they tend to agglomerate by the van der Waals forces in order to minimize their surface energies [14]. The mechanism behind the growth of CeO_2 reported in this work can be described as follows. For the MAH synthesis, the first step consists of preparing a solution containing Ce^{3+} and Co ions by dissolving the cerium nitrate and cobalt oxide,

respectively. The Ce^{3+} ions easily oxidize to Ce^{4+} during stirring due to the presence of dissolved O_2 in the solution. Then, the addition of OH^- instantly forms $Ce(OH)_4$ and $Co(OH)_3$ or $Co(OH)_2$ precipitates. Finally, microwave heating provides enough energy to deprotonate the rare-earth hydroxides and form the pure and Co-doped ceria nanocrystals. The anisotropic growth of ceria is dominated by Ostwald ripening and oriented attachment mechanisms. The literature shows that both mechanisms influence the growth of nanocrystals in hydrothermal processes, depending on the set of synthesis parameters. It is important to mention that ceria nanocrystals have extremely low solubility in water, which ends up hindering the dissolution-recrystallization (Ostwald ripening) mechanisms, especially if a high OH^- concentration is employed.

3.1.5. Positron annihilation lifetime spectroscopy (PALS)

When measuring different crystalline materials using PALS, generally from spectra decomposition, several lifetime components can be obtained, with each of them being characterized by a lifetime τ_i and its associated intensity I_i. The state i can represent the delocalized (bulk) state in the lattice or localized states at different defect sites where positrons become trapped and annihilated. In the latter case, the lifetime value reflects the size of the open volume associated with the vacancy-like defect in which positrons are annihilated (defect states). Therefore, an increase in lifetime means that positrons annihilate into bigger open volumes. Furthermore, their associated intensities I_i provide information about the defect concentrations. Correspondingly, an increase in I_i leads to an increment in the defect concentration.

From the measurement of the studied samples, it can be observed that the PALS spectra could be satisfactorily decomposed into three discrete lifetime components. As usual, the longest lifetime component, I_3, which has a value of 1500–2000 ps, is ascribed to an ortho-positronium (o-Ps) annihilation via the pick-off process in nanoholes [50]. The analysis of the PALS spectra obtained for all samples indicates very low values for the intensity associated with the o-Ps annihilation of this lifetime component, $\tau_{o-Ps}(I_3 = I_{o-Ps} < 1\%)$. Consequently, it can be concluded that the contribution of this lifetime component to the PALS spectra is almost negligible. Therefore, from now on this lifetime component will not be considered in the interpretation and discussion of PALS results. In order to fulfill the aim of the present work, it is considered that significant information on the defect structure of samples at the atomic scale can be obtained from the first and second lifetime components.

Table 3 presents the characteristic positron lifetime parameters obtained from the decomposition of the PALS spectra of the pure CeO_2 and Co-doped samples.

As it can be seen, the second lifetime component is dominant in the PALS spectra of the three samples. It is characterized by a constant positron lifetime $\tau_2 \sim 360ps$ that is within the experimental scatter and an associated intensity I_2 that systematically diminishes from 71% to
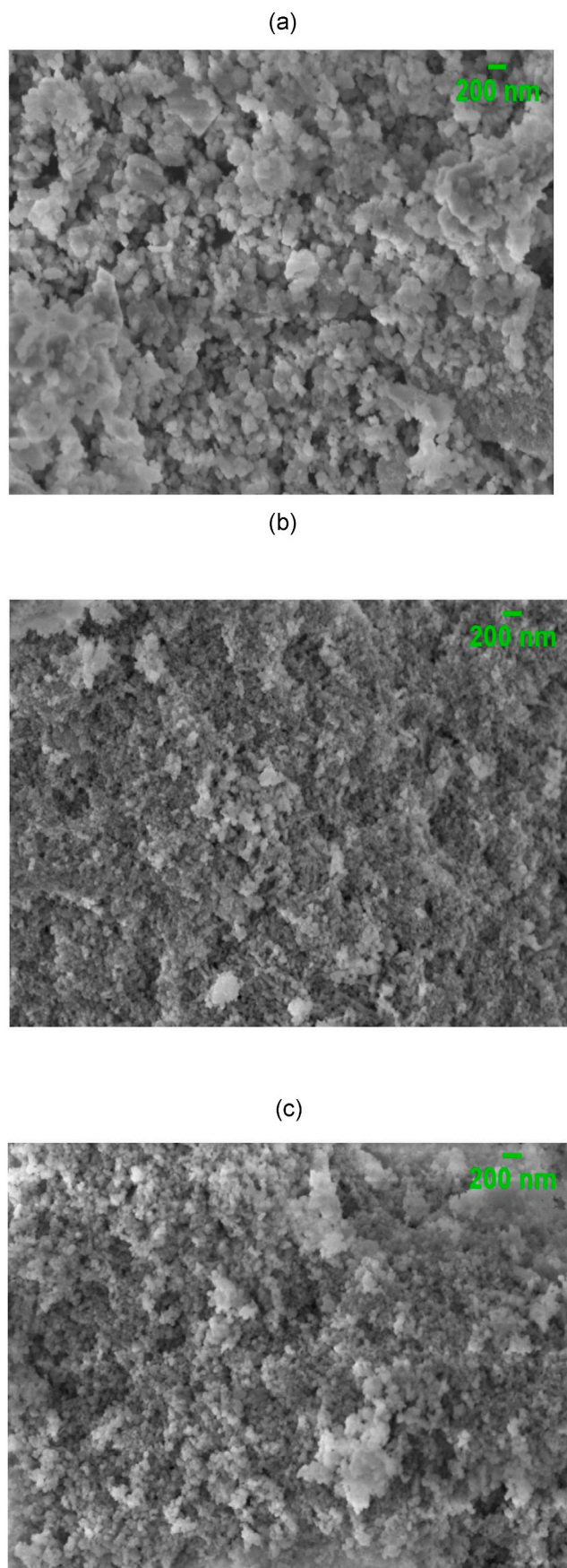
(a)

(b)

(c)

Fig. 5. Scanning electron microscopies of the (a) pure, (b) 4% wt, and (c) 12% wt. Co-doped CeO_2 nanopowders.

Table 2
Mean average sizes obtained by FEG-SEM images.

Sample	Mean Particle Size (nm)
CeO_2: Pure	50.15
CeO_2: 4% Co	47.73
CeO_2: 12% Co	43.24

Table 3
Values of positron lifetimes and their associated intensities obtained from the decomposition of PALS spectra for pure and Co-doped samples.

Sample	τ_1 (ps)	I_1 (%)	τ_2 (ps)	I_2 (%)
CeO_2: Pure	203 ± 2	29.0 ± 0.5	358 ± 5	71.0 ± 0.5
CeO_2: 4% Co	206 ± 2	31.5 ± 0.5	362 ± 5	68.5 ± 0.5
CeO_2: 12% Co	225 ± 3	39.2 ± 0.5	360 ± 5	60.8 ± 0.5

61% when the doping level increases. The opposite behavior is observed for the short-lived lifetime τ_1, which systematically increases from ~203 ps to ~225 ps.

As already reported by some authors of the present work and other researchers studying the defect structure of different CeO_2-based nanostructured systems [16,51–57] and its dependence on the synthesis route or the addition of different chemical elements, in the PALS spectra there is a dominant second lifetime component that can be ascribed to a positron annihilation in large oxygen vacancy clusters (OVCs) located on grain surfaces. In addition, the first lifetime component is related to positrons annihilating into small intragranular neutral complexes formed by a positive O vacancy and a negative ion such as $[Ce'_{Ce} \cdot V\ddot{O} \cdot Ce'_{Ce}]^X$ or $[RE'_{Ce} \cdot V_O \cdots RE']^X$, where RE refers to rare-earth elements [16,53,55–59]. In this context, the high I_2 values of the three samples presented in Table 3 can be attributed to positrons trapped and then annihilated in OVCs formed on the nanograin surfaces. Furthermore, the aforementioned reduction in I_2 with increasing the Co content in the ceria samples may be a result of the addition of Co to the CeO_2, which consequently induces a decrease in the OVC concentration, while the constancy of the τ_2 values for all samples indicates that the OVCs maintain their sizes regardless of the Co addition.

In the case of the first lifetime component reported in Table 3, for all measured samples the τ_1 values are systematically higher than those reported in the literature for defect-free pure CeO_2, $\tau_b = 185–187$ ps [53, 60], but lower than the reported lifetime values for positrons annihilated in V_O-negative complexes, which range from 236 ps to 277 ps [51,53,55, 60]. Accordingly, our τ_1 can be assigned to positrons annihilated in a mixed state containing defect-free CeO_2 and V_O-negative ion complexes. Moreover, the increase in the τ_1 values as a function of the Co doping level can be attributed to an increase in the concentration of V_O-negative ion complexes. A detailed description of this behavior is given by Hautojärvi and Corbel [61].

In summary, the PALS results indicate that the Co-doped CeO_2 nanograins contain neutral V_O-negative ion intragrain complexes and oxygen-vacancy clusters on their surfaces. With the addition of Co, the size of OVCs does not significantly change, whereas their concentrations systematically decrease. On the other hand, the concentration of V_O-negative ion complexes increases with increasing the Co doping level in ceria-based samples.

Besides, from the results shown in the Raman section (3.1.2) and the XPS section (3.1.3), we can conclude that the oxygen vacancies preferentially form near Co ions, thus reducing the Co ion charge and leading to the formation of neutral V_O-Co^{+2} complexes, as also proposed by Kikoin and Fleurov [62], Vodungbo et al. [63], and Ferrari et al. [64].
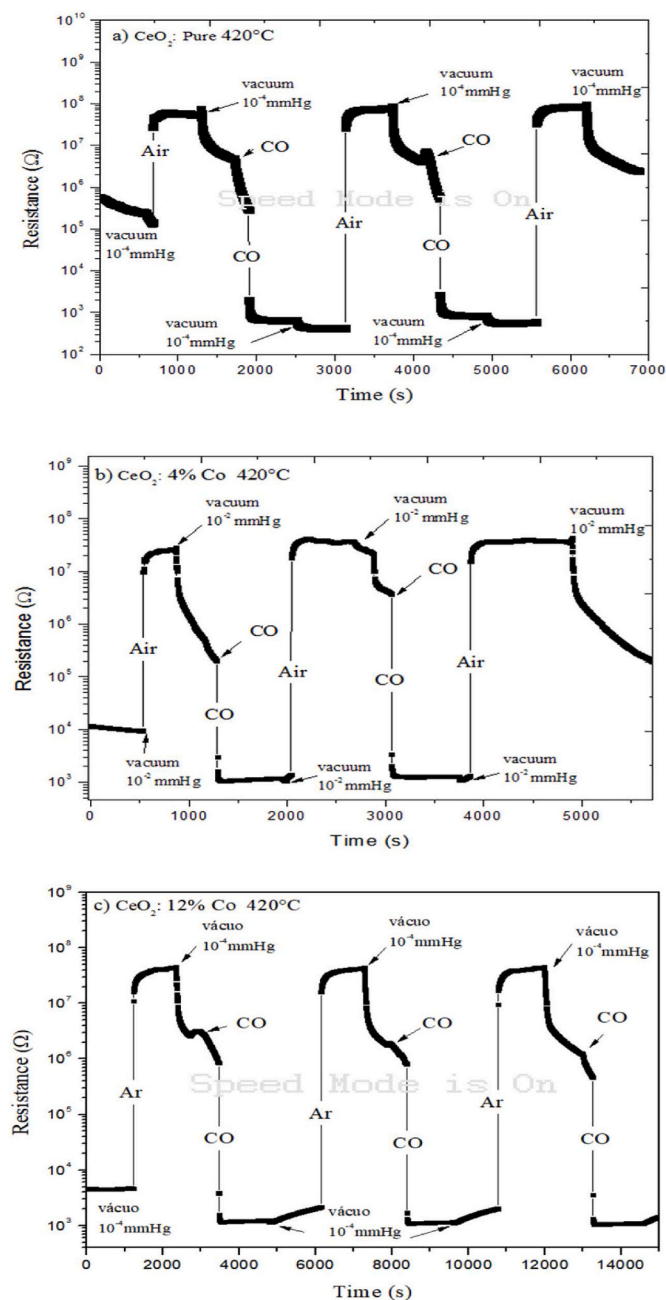
Fig. 6. Electrical measurements of resistance x time for the (a) pure, (b) 4% wt., and (c) 12% wt. doped films.

Fig. 7. ln (1/R) x 1/T plots for the pure, 4%, and 12% wt. doped samples under CO.

Table 4
Sensing behavior parameters under CO exposure.

Sample	T_{resp} (s)	T_{rec} (s)
CeO$_2$: Pure	98	24
CeO$_2$: 4% Co	3	16
CeO$_2$: 12% Co	485	254

3.2. Films characterization

3.2.1. Electrical characterization

After determining a working temperature of 420 °C, according to previous reports [4,15,65], the sensing behavior of the samples under carbon monoxide (CO), oxygen and vacuum atmospheres was measured (Fig. 6).
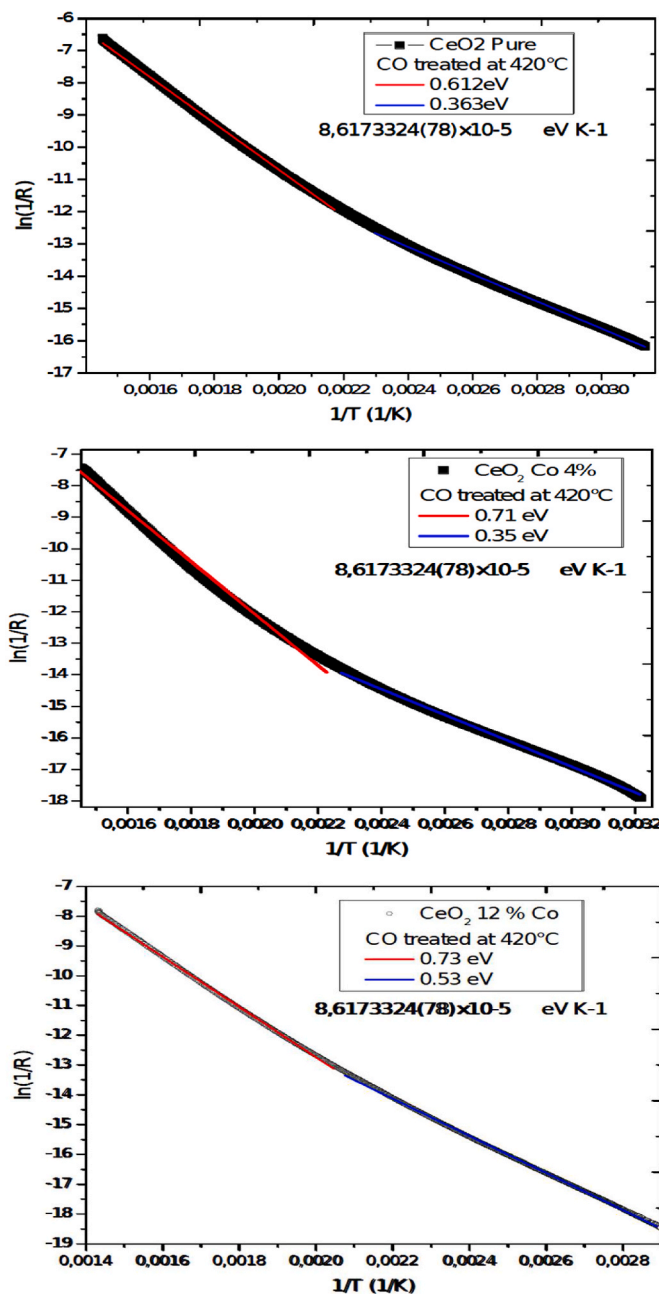
The sensing parameters, i.e., relative sensitivity (%) and response (T_{resp}) and recovery (T_{rec}) times, are presented in Table 4.

As it can be seen, the samples exhibited an n-type semiconductor behavior, as their resistance decreased due to CO introduction [66]. Since the cycles were reproducible, we used the first ones to measure the response and recovery times. In this regard, it is possible to observe that the pure system took 98 s to detect the presence of CO, while the response time of the 4 wt% Co-doped system was only 3 s, evidencing the strong influence of doping on the sensing capability of the films. In contrast, the 12 wt% Co-doped sample showed the highest response time, i.e., 485s. For comparison purposes, Amoresi et al. [67] prepared Ni2O3-decorated CeO2 nanoparticles by the MAH route and obtained response times for CO detection of 329 and 223 s under 5 and 50 mmHg of CO, respectively, at a temperature of 420 °C, corroborating the positive influence of cobalt doping on the sensing capability of ceria-based

Table 5
Activation energy values for the corresponding systems shown in Fig. 7.

Sample	Ea_1	Ea_2
CeO_2: Pure	0.612 eV	0.363 eV
CeO_2: 4% Co	0.710 eV	0.350 eV
CeO_2: 12% Co	0.730 eV	0.530 eV

materials. With respect to the deterioration of response and recovery times, the XPS results (Section 3.1.3) revealed a reduction of some cobalt ions from Co(III) to Co(II) in the sample doped with 12 wt% Co. This could be attributed both to the donation of electrons from these species to the neighboring oxygen vacancies and to their consequent annihilation, which caused a sudden decrease in the CO detection capability.

Regarding the low recovery times observed, the pure system took 24 s to return to its fundamental state, while the recovery time of the 4 wt%

Co-doped sample was only 16 s, evidencing the good influence of cobalt modification on the sensing capability of these systems. From the cycles seen in Fig. 6, one can also note the good reproducibility of the signal.

Similarly, Majumder and Roy [68] produced CeO_2 nanospheres with response times of 9, 10 and 13 sand recovery times of 11, 12 and 14 s under 10, 20 and 30 ppm of CO, respectively, besides a relative sensitivity ranging between 40 and 55%. These values confirm that cobalt modification is a good strategy to improve the sensing capability of CeO_2-based gas sensors.

Additionally, we were able to determine the activation energies for the sensing measurements under CO (Fig. 7) and their corresponding values (Table 5).

As observed, the samples indicated the presence of two distinct activation energies each, strongly suggesting the presence of an energetic level distribution, and consequently corroborating the
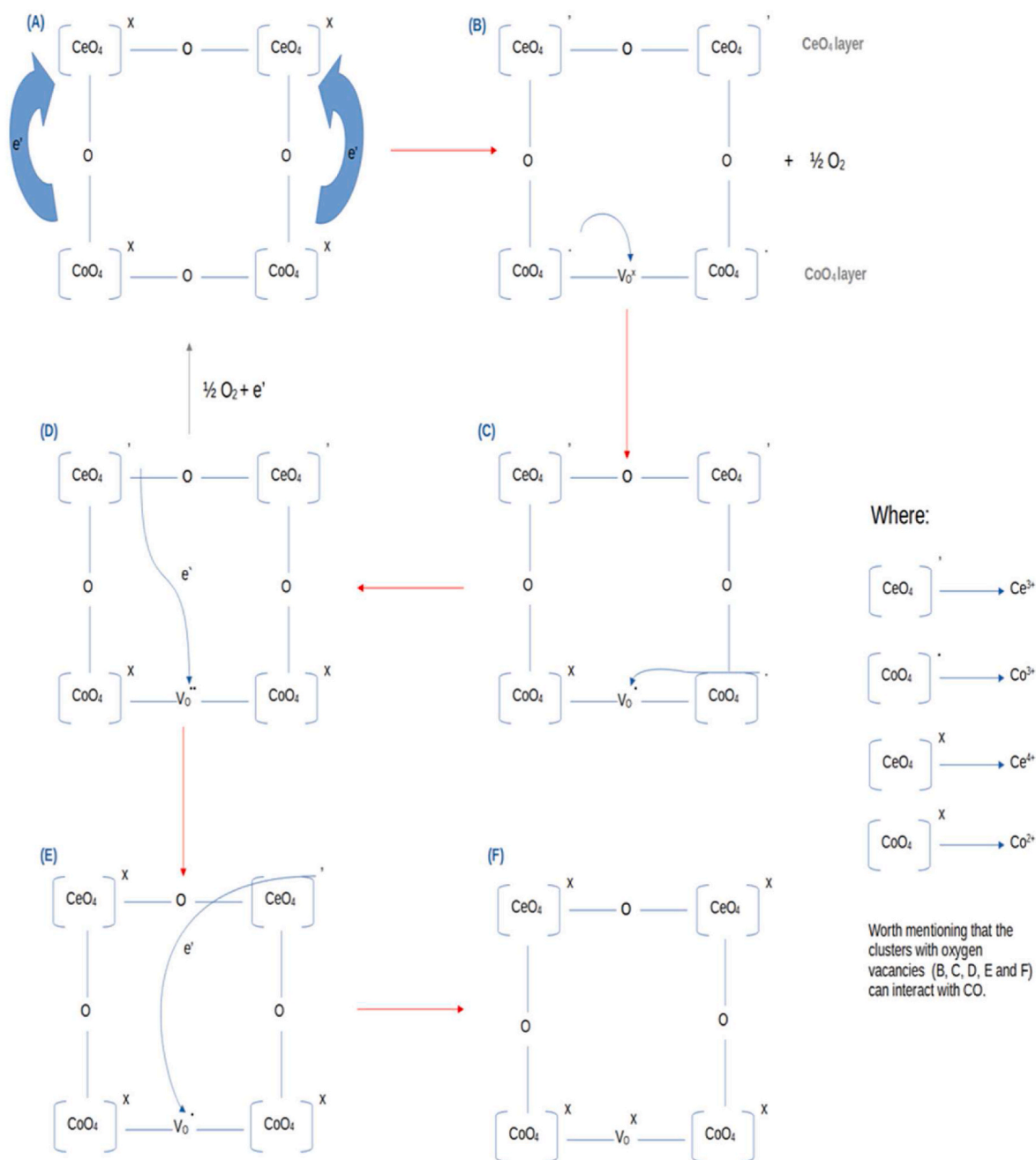

Fig. 8. Possibilities of charge density distribution and the generation of reduced Co^{2+} and Ce^{3+} species.

phenomenon of cluster-to-cluster charge transfer (CCCT) [16] supported by the hopping conduction mechanism along with the small polaron theory for nanostructured rare-earth based materials [24,69].

To better understand the variation and improvement of response and recovery times in the pure and doped samples followed by an extreme deterioration of their sensing capacity (Table 4), we proposed an hypothesis according to the Kroger–Vink notation [70,71] and the cluster-to-cluster charge transfer mechanism [72], as follows.

During the synthesis of cerium oxide with cobalt oxide, random vacancies are formed in the crystal structure. These vacancies will determine the semiconductor character of ceria, and will actively participate in the electron density distribution. This distribution involves complex clusters that form layers at short and medium ranges. For a more detailed comprehension, Fig. 8 shows the different possibilities of charge density distribution, namely: A) ceria doped with cobalt without defects in their structure; B) the formation of a vacancy due to the removal of an oxygen atom from the crystal lattice, with the consequent formation of Ce(+3) and Co(+3); C) the transfer of an electron to the cobalt cluster caused by a positively ionized oxygen vacancy; D) either the return to the original cluster structure (A) by transferring two electrons and reacting with oxygen, consequently eliminating the vacancy, or (E) the transfer of only one electron; and lastly, (F) the transfer of an electron, forming the neutral structure with vacancy.

4. Conclusion

Pure and Co-doped CeO_2 nanostructures with no impurities and secondary phases were produced by the microwave-assisted hydrothermal route. The Raman studies showed a shift of the primary mode towards lower energies with increasing the Co content, corroborating the presence of oxygen vacancies and their increased amount as a function of the dopant concentration. Regarding the optical band gap, the experimental values obtained in our study ranged between 3.24 and 3.35 eV, with an overall reduction as the doping agent content increased, evidencing the creation of oxygen vacancies and the reduction of Ce(IV) to Ce(III). The XPS measurements revealed the presence of 63% of Ce (IV) and 37% of Ce (III) states, kept virtually constant in all samples. The gas-sensing measurements showed a sudden reduction in the response and recovery times of the 4 wt% Co-doped system in comparison with the pure sample, followed by a deterioration of the sensing capacity of the 12 wt% sample due to a neutralization of oxygen vacancy species associated with the p-type semiconductor behavior of cobalt. Finally, the presence of distinct activation energies in the samples strongly suggested the influence of the cluster-to-cluster charge transfer (CCCT) mechanism with quantum origins on their electrical properties.

Declaration of competing interest

The authors declare the following financial interests/personal relationships which may be considered as potential competing interests:
Editor of Journal of Alloys and Compounds- V.R. Mastelaro.

Acknowledgments

Appendix A. Supplementary data

Supplementary data to this article can be found online at https://doi.org/10.1016/j.oceram.2022.100298.

References

[1] F. Liu, X. Lin, M. Zhang, Global, regional, and national burden of accidental carbon monoxide poisoning, 1990–2019: a systematic analysis for the global burden of disease study 2019, SSRN Electron. J. (2020) 1990–2019, https://doi.org/10.2139/ssrn.3745098.
[2] R.C. Deus, R.A.C. Amoresi, P.M. Desimone, et al., Electrical behavior of cerium dioxide films exposed to different gases atmospheres, Ceram. Int. 42 (2016) 15023–15029, https://doi.org/10.1016/j.ceramint.2016.06.151.
[3] H. Yan, P. Song, S. Zhang, et al., Facile synthesis, characterization and gas sensing performance of ZnO nanoparticles-coated MoS2 nanosheets, J. Alloys Compd. 662 (2016) 118–125, https://doi.org/10.1016/j.jallcom.2015.12.066.
[4] L.S.R. Rocha, M. Cilense, M.A. Ponce, et al., Novel gas sensor with dual response under CO(g) exposure: optical and electrical stimuli, Phys. B Condens. Matter 536 (2018) 280–288, https://doi.org/10.1016/j.physb.2017.10.083.
[5] V.L. Patil, S.A. Vanalakar, P.S. Patil, J.H. Kim, Fabrication of nanostructured ZnO thin films based NO2 gas sensor via SILAR technique, Sens. Actuators, B 239 (2017) 1185–1193, https://doi.org/10.1016/j.snb.2016.08.130.
[6] V.S. Bhati, M. Hojamberdiev, M. Kumar, Enhanced sensing performance of ZnO nanostructures-based gas sensors: a review, Energy Rep. 6 (2020) 46–62, https://doi.org/10.1016/j.egyr.2019.08.070.
[7] S. Hussain, N. Aslam, X.Y. Yang, et al., Unique polyhedron CeO2 nanostructures for superior formaldehyde gas-sensing performances, Ceram. Int. 44 (2018) 19624–19630, https://doi.org/10.1016/j.ceramint.2018.07.212.
[8] D.N. Oosthuizen, D.E. Motaung, H.C. Swart, Gas sensors based on CeO2 nanoparticles prepared by chemical precipitation method and their temperature-dependent selectivity towards H2S and NO2 gases, Appl. Surf. Sci. 505 (2020), 144356, https://doi.org/10.1016/j.apsusc.2019.144356.
[9] K. Reed, A. Cormack, A. Kulkarni, et al., Exploring the properties and applications of nanoceria: is there still plenty of room at the bottom? Environ Sci Nano 1 (2014) 390–405, https://doi.org/10.1039/C4EN00079J.
[10] M. Alaydrus, M. Sakaue, H. Kasai, A DFT+U study on the contribution of 4f electrons to oxygen vacancy formation and migration in Ln-doped CeO2, Phys. Chem. Chem. Phys. 18 (2016) 12938–12946, https://doi.org/10.1039/C6CP00637J.
[11] J. Calvache-Muñoz, F.A. Prado, J.E. Rodríguez-Páez, Cerium oxide nanoparticles: synthesis, characterization and tentative mechanism of particle formation, Colloids Surf. A Physicochem. Eng. Asp. 529 (2017) 146–159, https://doi.org/10.1016/j.colsurfa.2017.05.059.
[12] N.V. Skorodumova, S.I. Simak, B.I. Lundqvist, et al., Quantum origin of the oxygen storage capability of ceria, Phys. Rev. Lett. 89 (2002), https://doi.org/10.1103/PhysRevLett.89.166601.
[13] R.C. Deus, M. Cilense, C.R. Foschini, et al., Influence of mineralizer agents on the growth of crystalline CeO 2 nanospheres by the microwave-hydrothermal method, J. Alloys Compd. 550 (2013) 245–251, https://doi.org/10.1016/j.jallcom.2012.10.001.
[14] R.C. Deus, C.R. Foschini, B. Spitova, et al., Effect of soaking time on the photoluminescence properties of cerium oxide nanoparticles, Ceram. Int. 40 (2014) 1–9, https://doi.org/10.1016/j.ceramint.2013.06.043.
[15] P.P. Ortega, L.S.R. Rocha, J.A. Cortés, et al., Towards carbon monoxide sensors based on europium doped cerium dioxide, Appl. Surf. Sci. 464 (2019), https://doi.org/10.1016/j.apsusc.2018.09.142.
[16] R. Cristina de Oliveira, L. Cabral, A.C. Cabral, et al., Charge transfer in Pr-Doped cerium oxide: experimental and theoretical investigations, Mater. Chem. Phys. 249 (2020), https://doi.org/10.1016/j.matchemphys.2020.122967.
[17] R.A.C. Amoresi, R.C. Oliveira, N.L. Marana, et al., CeO2 nanoparticle morphologies and their corresponding crystalline planes for the photocatalytic degradation of organic pollutants, ACS Appl. Nano Mater. 2 (2019) 6513–6526, https://doi.org/10.1021/acsanm.9b01452.
[18] R.C. de Oliveira, R.A.C. Amoresi, N.L. Marana, et al., Influence of synthesis time on the morphology and properties of CeO2 nanoparticles: an experimental–theoretical study, Cryst. Growth Des. 20 (2020) 5031–5042, https://doi.org/10.1021/acs.cgd.0c00165.
[19] M. Greluk, M. Rotko, G. Słowik, S. Turczyniak-Surdacka, Hydrogen production by steam reforming of ethanol over Co/CeO2 catalysts: effect of cobalt content, J. Energy Inst. 92 (2019) 222–238, https://doi.org/10.1016/j.joei.2018.01.013.
[20] S. Malwadkar, P. Bera, C.V.V. Satyanarayana, Influence of cobalt on performance of Cu–CeO2 catalysts for preferential oxidation of CO, J. Rare Earths 38 (2020) 941–950, https://doi.org/10.1016/j.jre.2019.08.001.
[21] L.A. Villas-Bôas, DPF de Souza, Efeito da adição de óxido de cobalto na sinterização e propriedades elétricas da cerâmica Ce0,8Gd0,2O1,9 obtida a partir de nanopós, Cerâmica 60 (2014) 285–290, https://doi.org/10.1590/s0366-69132014000200019.
[22] K. Ackland, J.M.D. Coey, Room temperature magnetism in CeO2—a review, Phys. Rep. 746 (2018) 1–39, https://doi.org/10.1016/j.physrep.2018.04.002.
[23] E. Swatsitang, S. Phokha, S. Hunpratub, S. Maensiri, Characterization of Sm-doped CeO2 nanoparticles and their magnetic properties, Phys. B Condens. Matter 485 (2016) 14–20, https://doi.org/10.1016/j.physb.2016.01.002.
[24] L.S.R. Rocha, R.A.C. Amoresi, H. Moreno, et al., Novel approaches of nanoceria with magnetic, photoluminescent, and gas-sensing properties, ACS Omega 5 (2020) 14879–14889, https://doi.org/10.1021/acsomega.9b04250.
[25] T. Nishimura, Y. Tsutsumi, T. Ishii, et al., Effects of transition metal doping to cerium-oxides in thermal reduction reaction, IOP Conf. Ser. Mater. Sci. Eng. 835 (2020), https://doi.org/10.1088/1757-899X/835/1/012012.

[26] L. Zhou, X. Li, Z. Yao, et al., Transition-metal doped ceria microspheres with nanoporous structures for CO oxidation, Sci. Rep. 6 (2016) 1–7, https://doi.org/10.1038/srep23900.

[27] D. Giebel, J. Kansy, LT10 program for solving basic problems connected with defect detection, Phys. Procedia 35 (2012) 122–127, https://doi.org/10.1016/j.phpro.2012.06.022.

[28] N. Tibaldi, M.A. Ponce, P. Kalafatovich, et al., Dispositivo de caracterização optoeletrônica de materiais, 2016.

[29] N. Tibaldi, M.A. Ponce, P. Kalafatovich, et al., Un dispositivo de caracterización optoelectrónica de materiales, 2015.

[30] G. Hwang, J. Choi, Determination of crystal size and microstrain of CeO2 by Rietveld structure refinement, J. Mineral Soc. 21 (2008) 201–208.

[31] Y.A. Syed Khadar, A. Balamurugan, V.P. Devarajan, et al., Synthesis, characterization and antibacterial activity of cobalt doped cerium oxide (CeO 2 : Co) nanoparticles by using hydrothermal method, J. Mater. Res. Technol. 8 (2019) 267–274, https://doi.org/10.1016/j.jmrt.2017.12.005.

[32] J. Saranya, K.S. Ranjith, P. Saravanan, et al., Cobalt-doped cerium oxide nanoparticles: enhanced photocatalytic activity under UV and visible light irradiation, Mater. Sci. Semicond. Process. 26 (2014) 218–224, https://doi.org/10.1016/j.mssp.2014.03.054.

[33] S. George, J. Alex, L. Joy, et al., Nonlinear optical and photocatalytic dye degradation of Co doped CeO2 nanostructures synthesized through a modified combustion technique, Ceram. Int. 46 (2020), https://doi.org/10.1016/j.ceramint.2020.02.189.

[34] Y.M. Zhang, J.R.G. Evans, S. Yang, The prediction of solid solubility of Alloys: developments and applications of hume-rothery's rules, ChemInform 44 (2013), https://doi.org/10.1002/chin.201335198.

[35] P.A. Kumar, M.D. Tanwar, N. Russo, et al., Synthesis and catalytic properties of CeO 2 and Co/CeO 2 nanofibres for diesel soot combustion, Catal. Today 184 (2012) 279–287, https://doi.org/10.1016/j.cattod.2011.12.025.

[36] M. Gupta, A. Kumar, A. Sagdeo, P.R. Sagdeo, Doping-induced combined fano and phonon con fi nement E ff ect in La-doped CeO 2, Raman Spectrosc. Anal. (2021), https://doi.org/10.1021/acs.jpcc.0c09133.

[37] D. Jampaiah, P. Venkataswamy, V.E. Coyle, et al., Low-temperature CO oxidation over manganese, cobalt, and nickel doped CeO2 nanorods, RSC Adv. 6 (2016) 80541–80548, https://doi.org/10.1039/C6RA13577C.

[38] J.R. McBride, K.C. Hass, B.D. Poindexter, W.H. Weber, Raman and x-ray studies of Ce1−xRExO2−y, where RE=La, Pr, Nd, Eu, Gd, and Tb, J. Appl. Phys. 76 (1994) 2435–2441, https://doi.org/10.1063/1.357593.

[39] A.A. Fauzi, A.A. Jalil, N.S. Hassan, et al., A critical review on relationship of CeO2-based photocatalyst towards mechanistic degradation of organic pollutant, Chemosphere 286 (2022), https://doi.org/10.1016/j.chemosphere.2021.131651.

[40] G. Vinothkumar, R. Amalraj, K.S. Babu, Fuel-oxidizer ratio tuned luminescence properties of combustion synthesized Europium doped cerium oxide nanoparticles and its effect on antioxidant properties, Ceram. Int. 43 (2017) 5457–5466, https://doi.org/10.1016/j.ceramint.2017.01.053.

[41] J.E. Spanier, R.D. Robinson, F. Zhang, et al., Size-dependent properties of (formula presented) nanoparticles as studied by Raman scattering, Phys. Rev. B Condens. Matter 64 (2001), https://doi.org/10.1103/PhysRevB.64.245407.

[42] K.I. Maslakov, Y.A. Teterin, A.J. Popel, et al., XPS study of ion irradiated and unirradiated CeO2bulk and thin film samples, Appl. Surf. Sci. 448 (2018) 154–162, https://doi.org/10.1016/j.apsusc.2018.04.077.

[43] K.I. Maslakov, Y.A. Teterin, M.V. Ryzhkov, et al., The electronic structure and the nature of the chemical bond in CeO2, Phys. Chem. Chem. Phys. 20 (2018) 16167–16175, https://doi.org/10.1039/C8CP01442F.

[44] D. Channei, B. Inceesungvorn, N. Wetchakun, et al., Photocatalytic degradation of methyl orange by CeO2 and Fe–doped CeO2 films under visible light irradiation, Sci. Rep. 4 (2014) 5757, https://doi.org/10.1038/srep05757.

[45] K.M. Dunnick, R. Pillai, K.L. Pisane, et al., The effect of cerium oxide nanoparticle valence state on reactive oxygen species and toxicity, Biol. Trace Elem. Res. 166 (2015) 96–107, https://doi.org/10.1007/s12011-015-0297-4.

[46] M.M. Natile, A. Glisenti, Nanostructured CeO2 powders by XPS, Surf. Sci. Spectra 13 (2006) 17–30, https://doi.org/10.1116/11.20060401.

[47] L. Truffault, M.-T. Ta, T. Devers, et al., Application of nanostructured Ca doped CeO 2 for ultraviolet filtration, Mater. Res. Bull. 45 (2010) 527–535, https://doi.org/10.1016/j.materresbull.2010.02.008.

[48] E. Heckert, A. Karakoti, S. Seal, W.T. Self, The role of cerium redox state in the SOD mimetic activity of nanoceria, Biomaterials 29 (2008) 2705–2709.

[49] P.W. Menezes, A. Indra, V. Gutkin, M. Driess, Boosting electrochemical water oxidation through replacement of Oh Co sites in cobalt oxide spinel with manganese, Chem. Commun. 53 (2017) 8018–8021, https://doi.org/10.1039/C7CC03749J.

[50] R. Krause-Rehberg, H.S. Leipner, Positron Annihilation in Semiconductors, 1999.

[51] L. Xiangwen, Z. Kebin, W. Lei, et al., Oxygen vacancy clusters promoting reducibility and activity of ceria nanorods, J. Am. Chem. Soc. 131 (2009) 3140–3141.

[52] S. Chang, M. Li, Q. Hua, et al., Shape-dependent interplay between oxygen vacancies and Ag-CeO 2 interaction in Ag/CeO 2 catalysts and their influence on the catalytic activity, J. Catal. 293 (2012) 195–204, https://doi.org/10.1016/j.jcat.2012.06.025.

[53] A.V. Thorat, T. Ghoshal, J.D. Holmes, et al., A positron annihilation spectroscopic investigation of europium-doped cerium oxide nanoparticles, Nanoscale 6 (2014) 608–615, https://doi.org/10.1039/C3NR03936F.

[54] K. Sato, Grain-boundary structures associated with ionic transport in Gd-doped ceria nanostructured electrolyte, J. Phys. Chem. C 119 (2015) 5734–5738, https://doi.org/10.1021/acs.jpcc.5b00155.

[55] K. Sudarshan, V. Tiwari, P. Utpalla, S.K. Gupta, Defect evolution in Eu3+, Nb5+ doped and co-doped CeO2: X-ray diffraction, positron annihilation lifetime and photoluminescence studies, Inorg. Chem. Front. 6 (2019) 2167–2177, https://doi.org/10.1039/C9QI00668K.

[56] I.C.F. Vaz, C.E. Macchi, A. Somoza, et al., Electrical transport mechanisms of Neodymium-doped rare-earth semiconductors, J. Mater. Sci. Mater. Electron. (2022), https://doi.org/10.1007/s10854-022-08098-9.

[57] L.S.R. Rocha, A.Z. Simões, C. Macchi, et al., Synthesis and defect characterization of hybrid ceria nanostructures as a possible novel therapeutic material towards COVID-19 mitigation, Sci. Rep. 12 (2022) 3341, https://doi.org/10.1038/s41598-022-07200-9.

[58] X. Liu, K. Zhou, L. Wang, et al., Oxygen vacancy clusters promoting reducibility and activity of ceria nanorods, J. Am. Chem. Soc. 131 (2009) 3140–3141, https://doi.org/10.1021/ja808433d.

[59] A. Sachdeva, S.V. Chavan, A. Goswami, et al., Positron annihilation spectroscopic studies on Nd-doped ceria, J. Solid State Chem. 178 (2005) 2062–2066, https://doi.org/10.1016/j.jssc.2005.04.016.

[60] A. Sachdeva, S.V. Chavan, A. Goswami, et al., Positron annihilation spectroscopic studies on Nd-doped ceria, J. Solid State Chem. 178 (2005) 2062–2066, https://doi.org/10.1016/j.jssc.2005.04.016.

[61] P. Hautojärvi, C. Corbel, Positron spectroscopy of defects in metals and semiconductors, in: Positron Spectroscopy of Solids, 1995, pp. 491–532.

[62] K. Kikoin, V. Fleurov, Superexchange in dilute magnetic dielectrics: application to (Ti,Co)O2, Phys. Rev. B 74 (2006), 174407, https://doi.org/10.1103/PhysRevB.74.174407.

[63] B. Vodungbo, F. Vidal, Y. Zheng, et al., Structural, magnetic and spectroscopic study of a diluted magnetic oxide: Co doped CeO2−δ, J. Phys. Condens. Matter 20 (2008), 125222 https://doi.org/10.1088/0953-8984/20/12/125222.

[64] V. Ferrari, A.M. Llois, V. Vildosola, Co-doped ceria: tendency towards ferromagnetism driven by oxygen vacancies, J. Phys. Condens. Matter 22 (2010), 276002, https://doi.org/10.1088/0953-8984/22/27/276002.

[65] S.M.A. Durrani, M.F. Al-Kuhaili, I.A. Bakhtiari, Carbon monoxide gas-sensing properties of electron-beam deposited cerium oxide thin films, Sensor. Actuator. B Chem. 134 (2008) 934–939, https://doi.org/10.1016/j.snb.2008.06.049.

[66] A. Mirzaei, G. Neri, Microwave-assisted synthesis of metal oxide nanostructures for gas sensing application: a review, Sens. Actuators, B 237 (2016) 749–775, https://doi.org/10.1016/j.snb.2016.06.114.

[67] R.A. Ciola Amoresi, R. Cristina de Oliveira, L. Cichetto, et al., Pure and Ni2O3-decorated CeO2 nanoparticles applied as CO gas sensor: experimental and theoretical insights, Ceram. Int. 48 (2022) 14014–14025, https://doi.org/10.1016/j.ceramint.2022.01.286.

[68] D. Majumder, S. Roy, Development of low-ppm CO sensors using pristine CeO2 nanospheres with high surface area, ACS Omega 3 (2018) 4433–4440, https://doi.org/10.1021/acsomega.8b00146.

[69] L.S.R. Rocha, F. Schipani, C.M. Aldao, et al., Experimental and ab initio studies of deep-bulk traps in doped rare-earth oxide thick films, J. Phys. Chem. C 124 (2020) 997–1007, https://doi.org/10.1021/acs.jpcc.9b07217.

[70] F.A. Kröger, H.J. Vink, Relations between the concentration of imperfections in solids, J. Phys. Chem. Solid. 5 (1958) 208–223.

[71] F. Kröger, H. Vink, Physico-chemical properties of diatomic crystals in relation to the incorporation of foreign atoms with deviating valency, Physica 3 (1954) 950–964, https://doi.org/10.1016/S0031-8914(54)80305-3.

[72] A.E. Souza, G.S. Sasaki, S.A. Camacho, et al., Defects or charge transfer: different possibilities to explain the photoluminescence in crystalline Ba(ZrxTi1−x)O3, J. Lumin. 179 (2016) 132–138, https://doi.org/10.1016/j.jlumin.2016.06.033.